Mapping ground surface deformation using temporarily coherent point SAR interferometry: Application to Los Angeles Basin

Lei Zhang [a], Zhong Lu [b,*], Xiaoli Ding [a], Hyung-sup Jung [c], Guangcai Feng [a], Chang-Wook Lee [c]

[a] *The Hong Kong Polytechnic University, Hung Hom, KLN, Hong Kong*
[b] *U.S. Geological Survey, Vancouver, Washington, USA*
[c] *The University of Seoul, Seoul, Republic of Korea*

ABSTRACT

Multi-temporal interferometric synthetic aperture radar (InSAR) is an effective tool to detect long-term seismotectonic motions by reducing the atmospheric artifacts, thereby providing more precise deformation signal. The commonly used approaches such as persistent scatterer InSAR (PSInSAR) and small baseline subset (SBAS) algorithms need to resolve the phase ambiguities in interferogram stacks either by searching a predefined solution space or by sparse phase unwrapping methods; however the efficiency and the success of phase unwrapping cannot be guaranteed. We present here an alternative approach – temporarily coherent point (TCP) InSAR (TCPInSAR) – to estimate the long term deformation rate without the need of phase unwrapping. The proposed approach has a series of innovations including TCP identification, TCP network and TCP least squares estimator. We apply the proposed method to the Los Angeles Basin in southern California where structurally active faults are believed capable of generating damaging earthquakes. The analysis is based on 55 interferograms from 32 ERS-1/2 images acquired during Oct. 1995 and Dec. 2000. To evaluate the performance of TCPInSAR on a small set of observations, a test with half of interferometric pairs is also performed. The retrieved TCPInSAR measurements have been validated by a comparison with GPS observations from Southern California Integrated GPS Network. Our result presents a similar deformation pattern as shown in past InSAR studies but with a smaller average standard deviation (4.6 mm) compared with GPS observations, indicating that TCPInSAR is a promising alternative for efficiently mapping ground deformation even from a relatively smaller set of interferograms.

Published by Elsevier Inc.

1. Introduction

The Los Angeles Basin, a polyphase Neogene basin within the San Andreas transform system, has been developed as a result of regional crustal extension associated with the opening of the California Borderlands and the rotation of the Transverse Ranges (Fig. 1) (Davis, Namson, & Yerkes, 1989; Hauksson, 1990; Shaw & Suppe, 1996; Wald and Graves, 1998; Wright, 1991; Yerkes, McCulloh, Schoellhamer, & Vedder, 1965). Since the early Pliocene, the basin has been deformed by numerous decoupled strike–slip and thrust motions within several active fault zones that are capable of generating moderate to large earthquakes. Studies of historic earthquakes including the 1933 Long Beach (Mw = 6.4), 1971 San Fernando (Mw = 6.7), 1987 Whittier Narrows (Mw = 6.0), and 1994 Northridge (Mw = 6.7) (Fig. 1) revealed that both surface and blind thrust faults represent a significant threat to the Los Angeles metropolitan area (Bawden, Thatcher, Stein, Hudnut, & Peltzer, 2001; Davis et al., 1989; Hauksson, 1987; Hauksson

& Jones, 1989; Hauksson, Jones, & Hutton, 1995; Mellors, Magistrale, Earle, & Cogbill, 2004; Shaw & Shearer, 1999). Hence, understanding the seismotectonic motions in the Los Angeles Basin is important for assessing and mitigating earthquake hazards.

The use of multi-temporal interferometric SAR (InSAR) technique to determine ground motions is becoming an increasingly important approach to the evaluation of interseismic strain accumulation in seismic zones (Biggs, Wright, Lu, & Parsons, 2007; Fialko, 2004; Lanari, Lundgren, Manzo, & Casu, 2004a; Li, Fielding, & Cross, 2009). Compared with GPS observations, the high spatial-resolution of InSAR measurements can better constrain surface deformation in the regions characterized by complex faulting. On the other hand, we have to realize that InSAR cannot have the temporal resolution as high as GPS observations and has difficulties in resolving seasonal variations. Several multi-temporal analysis methods have been developed, all of which basically fall into three categories. The first deals with single master based interferograms such as PSInSAR (Ferretti, Prati, & Rocca, 2000, 2001), and STUN (Kampes, 2006). The second consists of approaches based on multi-master interferograms such as stacking analysis (Lu, Dzurisin, Biggs, Wicks, & McNutt, 2010; Wright, Parsons, & Fielding, 2001), small baseline subset (SBAS)
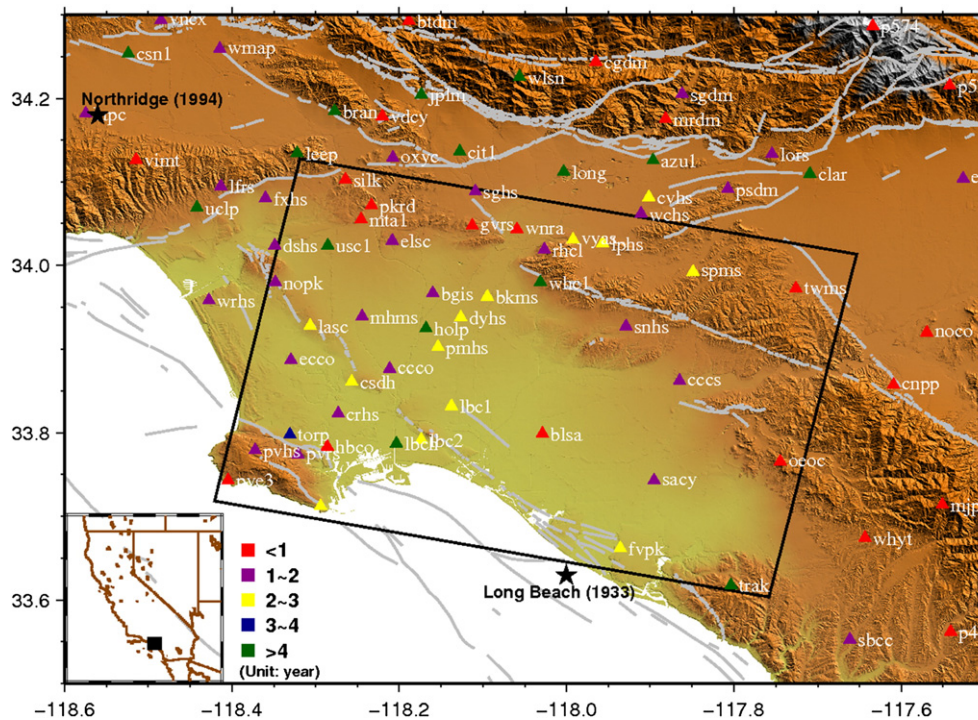
Fig. 1. Shaded relief map of the Los Angeles Basin. Faults appear as gray lines (data source: (U.S. Geological Survey, 2010)). The black box outlines the studied area covered by ERS-1/2 SAR data (track 170, frame 2925). The triangles indicate the location of GPS sites of SIGN and the corresponding colors show the overlap time with the SAR data (unit: year).The black stars represent the moderate-size earthquakes occurred in the basin.

(Berardino, Fornaro, Lanari, & Sansosti, 2002; Lanari et al., 2004b), and CPT (Blanco, Mallorquí, Duque, & Monells, 2008; Mora, Mallorquí, & Broquetas, 2003). The last category is the integration of single- and multi-master interferogram analysis such as StaMPS (Hooper, 2008). One significant limitation of these methods, however, is that phase unwrapping, a required processing procedure, cannot be always successfully performed. In the PSInSAR and CPT, as a non-linear inversion problem, the parameters are estimated by searching a predefined solution space to maximize the model coherence. The search of solution, which is essentially a phase unwrapping process, is performed arc by arc, leading to a low efficiency. Moreover, the method might result in several local maxima during the parameter search, which means a unique solution cannot be guaranteed. In the SBAS method, 2D phase unwrapping of sparsely coherent points is sometimes challenging due to phase discontinuities (Lauknes et al., 2011). In this paper, we present a new multi-temporal InSAR analysis method, named as temporally coherent point (TCP) InSAR (TCPIn-SAR), to derive long-term deformation rate. The proposed method utilizes a well-known fact that there are usually sufficient arcs constructed by two neighboring coherent pixels in interferograms with short baselines (spatial, temporal and Doppler) that do not have phase ambiguities. TCPInSAR only employ arcs without phase ambiguities to retrieve deformation signals, which includes a series of innovations such as TCP identification (Zhang, Ding, & Lu, 2011a), TCP networking and TCP least squares estimator (Zhang et al., 2011b). With TCPInSAR, coherent points can be selected from a small set of interferograms and the deformation rate can be estimated without the need of phase unwrapping since the arcs with modulo-2π ambiguities can be reliably detected and removed. For the sake of comparison, a technical summary of current multi-temporal InSAR methods is presented in Table 1.

The proposed method is applied to the Los Angeles Basin where moderate tectonic movements and minimum image decorrelation make it very suitable for testing novel InSAR techniques (Bawden et al., 2001; Brooks et al., 2007; Colesanti, Ferretti, Prati, & Rocca, 2003; Lanari et al., 2004a). Compared with Zhang et al. (2011b) where only simulated data were employed to validate the least squares estimator, processing details related to the application of TCPInSAR to real datasets (ERS-1/2 images) are provided in this paper. Technical issues are addressed to deal with the problem of phase jumps at interferometric fringe edges as well as the effect of arc length on estimating spatially and temporally complex deformation. Moreover the estimation of deformation time series without a priori model is also performed. The estimated linear deformation rate and time-series deformation histories from ERS-1/2 data covering the period of Oct. 1995 to Dec. 2000 are in good agreement with

Table 1
Comparison among current multi-temporal InSAR techniques.

Techniques	Interferogram type	Observation type	Observation with ambiguities	Point selection	Parameter solver
PSInSAR	Single-master	Arc (point pair)	Yes	Amplitude dispersion index	Model coherence maximization
STUN	Single-master	Arc (point pair)	Yes	Signal to clutter radio	Weighted integer least squares
StaMPS	Single/multimaster	Arc (point pair)	Yes	Phase stability	3D unwrapping
SBAS	Multi-master	Point	No[a]	Coherence	Minimum norm least squares
CPT	Multi-master	Arc (point pair)	Yes	Coherence and amplitude dispersion index	Model coherence maximization
TCPInSAR	Multi-master	Arc (point pair)	No[b]	Offset deviation	Least squares with ambiguity detector

[a] The starting point of SBAS is the unwrapped interferograms.
[b] Observations with phase ambiguities can be detected and removed in TCPInSAR.

GPS observations from Southern California Integrated GPS Network (SCIGN) and past InSAR results with phase unwrapping (Bawden et al., 2001; Brooks et al., 2007; Casu, Manzo, & Lanari, 2006; Colesanti et al., 2003; Lanari et al., 2004a; Watson, Bock, & Sandwell, 2002). Moreover, to evaluate the performance of our model with smaller datasets, we have applied the TCPInSAR approach with half of the original interferometric observations. The estimated line-of-sight (LOS) linear deformation rate is consistent with the one estimated from the full dataset. Quantitative comparisons have confirmed the validity of the results achieved from the TCPInSAR method, indicating the TCPInSAR has the potential to provide ground motion data for fault stress inversion and seismic hazard evaluation with significantly reduced computational complexity even in areas without abundant SAR images.

2. Method

2.1. Data selection

We wish to reduce the phase contribution related to topography residuals, atmospheric artifacts as much as possible so that phase differences at sufficient arcs in a limited time span will not have modulo-2π ambiguities. To this end, we only select image pairs with spatial perpendicular baselines of less than ~300 m and temporal baselines of less than ~2.5 year (Fig. 2). In addition, the Doppler centroid frequency differences in the selected pairs are within 300 Hz so that we can model the phase difference caused by the azimuth sub-pixel positioning at two neighboring points as a random component in a large set of interferograms. We further remove the interferograms that are obviously affected by the rather localized bubble-like atmospheric errors. Finally we select 55 interferograms from 32 ERS-1/2 images (track 170, frame 2925) as the basis of TCPInSAR processing.

2.2. TCP identification and coregistration

Temporarily coherent points (TCPs) are points in the interferograms that maintain coherence during one or several intervals of SAR acquisitions. However, it is not necessary for TCPs to be visible over the whole time span. The TCPs can primarily be identified based on the offset deviation in range and azimuth directions. The equation derived by Bamler and Eineder (2005) indicates that standard errors of the estimated offsets from stronger scatterers are less sensitive to the window size and oversampling factor used in the image cross-correlation compared with those from distributed scatterers. Therefore it is possible to distinguish the strong scatterers from distributed scatterers by offset statistics. The detailed analysis and test of the method can be found in Zhang et al. (2011a). Here we propose an improved processing strategy which can significantly accelerate TCP selection. Using the master image, we first identify points that can keep almost the same backscattering intensity when processed with fractional azimuth and range bandwidth as TCP candidates. Second, TCP candidates are further evaluated by changing the size of patches and the oversampling factor in image cross-correlation. For the sake of simplicity, a fixed oversampling factor can be used. We can then obtain an offset vector (OT_j) for a given TCP candidate (j) which includes the offsets (ot_{ji}, $i = 1, \cdots, N$) estimated from N windows with changing sizes as shown in Eq. (1). Points whose standard errors of offsets are less than a threshold are selected as TCP candidates. The threshold can be set as 0.1 considering the fact that the coregistration error would be negligible when the precision of calculated offsets reaches 0.1 pixel or better (Hanssen, 2001).

$$OT_j = \begin{bmatrix} ot_{j1} & ot_{j2} & \cdots & ot_{jN} \end{bmatrix}$$
$$std\left(OT_j\right) < 0.1 \tag{1}$$

Third, a high-order polynomial estimated by iteratively reweighted least squares is used to fit the offsets of TCP candidates and the final TCPs are selected by discarding pixels whose residual offsets are larger than 0.1 pixel after the polynomial fitting.

The precise offsets at TCPs are actually the by-product of TCP identification. If we coregister the slave images based on the polynomial determined from TCP offsets, the coregistration quality can be improved compared with the conventional coregistration method that
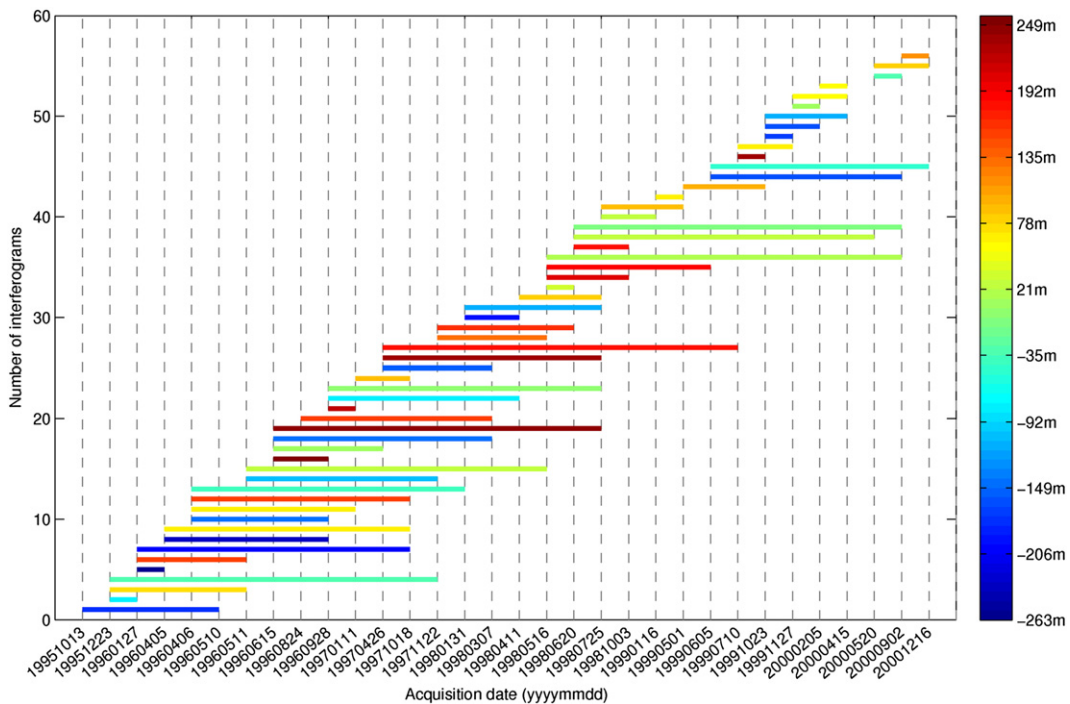

Fig. 2. Perpendicular spatial baselines and temporal intervals of the selected InSAR image pairs which are indicated by the color and length of the lines respectively.

uses offsets estimated from evenly distributed windows over the whole image. Especially in areas where the TCPs are surrounded by distributed scatterers, like the airport reclaimed from the sea (Zhang et al., 2011a) and long cross-sea bridges, the improvement of interferometric coherence resulted from TCP coregistration procedure is apparent. Over Los Angeles Basin, an average improvement of 0.05 with a standard deviation of 0.04 in interferometric coherence has been gained from TCP coregistration. It should be noted that since a TCP is selected based on image pairs, it can represent two types of point. If it keeps coherence in all image pairs, it can be called a persistently coherent point, while if it only keeps coherence in a subset of image pairs, it is a partially coherent point (Biggs et al., 2007, Biggs et al., 2009). In this work we only use the TCPs that are persistently coherent during the whole time span in order to retrieve the full resolution deformation time series. The application of TCPInSAR on changing landscapes where both persistently and partially coherent points are present can be found in (Zhang et al., 2011c).

2.3. TCP network and phase jump

Phase differences at arcs constructed from two neighboring pixels are the basic observations for the following least squares estimator. The differencing operation between two neighboring TCPs can reduce the part of atmospheric errors that are spatially correlated. In order to ensure that TCPs are connected extensively and there are sufficient arcs without phase ambiguity, we construct the network by local Delaunay triangulation that places regular patches over the image and connects the TCPs in each patch if the number of TCPs in the patch is larger than 3. A factor that should be addressed here is the arc length that is vital to reduce the atmospheric artifact and model the relative motion at arcs especially in the areas where the deformation pattern is spatially and temporally complex. The GPS observations and hydrological studies suggest that the deformation pattern in the Los Angeles Basin is rather complex which includes the tectonic motion as well as the variations of ground water table (Argus, Heflin, Peltzer, Crampe, & Webb, 2005; Bawden et al., 2001; Watson et al., 2002). The identified coherent points in the study area are abundant and can be connected extensively with short arcs. It has been found that the sensitivity of phase difference to seasonal fluctuations is less at shorter arcs than longer ones (Fig. 3). When estimating linear deformation rate under the framework of least squares, shorter arcs will result in less residuals than longer arcs. Using this procedure, we have identified 201,778 TCPs and constructed 1,176,922 arcs of less than 500 m for this study.

When determining the phase difference at arcs in the network, we should pay attention to the so-called "phase jumps" at interferometric fringe edges, which are caused by the fact that the observed interferometric phase is limited to a scope of $(-\pi \quad \pi]$. Considering two nearby points whose phase values of $\varphi_{1, true}$ and $\varphi_{2, true}$ are near the interferometric fringe edge as indicated in (2), where Δ_1 and Δ_2 are the small values and $\Delta_1 + \Delta_2$ is less than π. The direct phase difference between these two points is $-2\pi + \Delta_1 + \Delta_2$, where a modulo-$2\pi$ is artificially raised compared with its true differential value. Therefore a wrapping operation should be performed to eliminate this artificial error.

$$
\begin{aligned}
\varphi_{1,true} &= -\pi + \Delta_1 \\
\varphi_{2,true} &= -\pi - \Delta_2 \\
\varphi_{1,true} - \varphi_{2,true} &= \Delta_1 + \Delta_2 \in (-\pi \quad \pi] \\
\varphi_{1,observed} &= \varphi_{1,true} \\
\varphi_{2,observed} &= \pi - \Delta_2 \\
\varphi_{1,observed} - \varphi_{2,observed} &= -2\pi + \Delta_1 + \Delta_2 \\
wrap\left(\varphi_{1,observed} - \varphi_{2,observed}\right) &= \varphi_{1,true} - \varphi_{2,true} = \Delta_1 + \Delta_2
\end{aligned}
\tag{2}
$$

The difference between the observed phase difference and the wrapped phase at arcs (Fig. 4) where the values are represented by
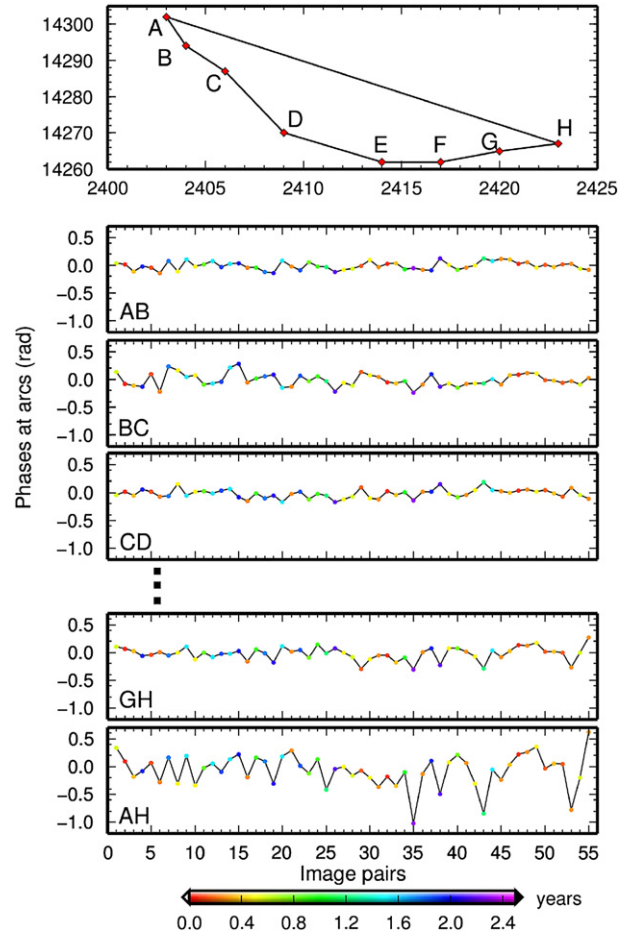

Fig. 3. The top figure shows the spatial location of TCPs. The rest of the figure shows the phase differences at short arcs (A–B–C–D–E–F–G) and a long arc (AH) in 55 selected interferograms.
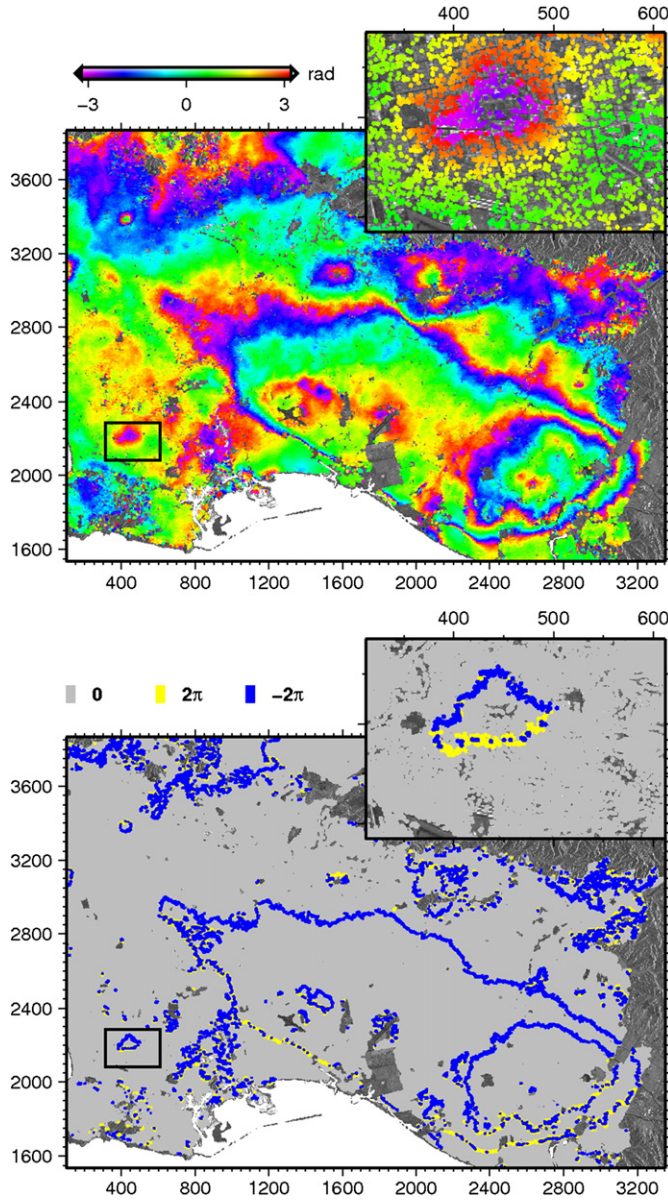
the middle points of the arcs clearly shows that all phase jumps occurred at arcs near the interferometric fringe edges. It should be noted that although the wrapping operation can remove the phase jumps at the fringe edges, it has a risk to raise a phase ambiguity to some of the arcs at which the true phase differences locate outside of $(-\pi \quad \pi]$. However these arcs can be identified and removed according to the residuals that arose from the least squares estimator in Section 2.4.

2.4. TCP least squares estimator

2.4.1. Linear deformation rate estimation

By selecting interferograms with relatively short spatial and temporal baselines and connecting TCPs with short arcs (less than 500 m) there will be no phase ambiguity at most arcs. The deformation rate can then be easily estimated under the framework of least squares, which has been discussed and tested with simulated data in Zhang et al. (2011b). We recall the model briefly here by considering $J+1$ SAR images acquired in an ordered time sequence $(t_0 \quad t_1 \quad \cdots \quad t_J)$ and I interferograms of short baselines. The phase difference $(\Delta\phi^i_{l, m, l', m'})$ at the arc constructed by TCP (l, m) and TCP (l', m') can be expressed as

$$
\begin{aligned}
\Delta\phi^i_{l,m,l',m'} &= \alpha^i_{l,m} \Delta h_{l,m,l',m'} + \beta_i \Delta V + w^i_{l,m,l',m'} \\
w^i_{l,m,l',m'} &= \Delta\phi^i_{atmo,l,m,l',m'} + \Delta\phi^i_{orbit,l,m,l',m'} + \Delta\phi^i_{dop,l,m,l',m'} + \Delta\phi^i_{noise,l,m,l'm'}
\end{aligned}
\tag{3}
$$

Fig. 4. (Top) A SAR interferogram of 19960406–19971018 under the SAR coordinate (unit: pixel of 20 m) and (bottom) phase jumps near the interferometric fringe edges.

$E(w_{l,\,m,\,l',\,m'}^i) = 0$. We can get the system of observations for arcs without phase ambiguities

$$\Delta\Phi = A\begin{bmatrix} \Delta h_{l,m,l',m'} \\ \Delta V \end{bmatrix} + W$$

$$\Delta\Phi = \begin{bmatrix} \Delta\phi_{l,m,l',m'}^1 & \Delta\phi_{l,m,l',m'}^2 & \cdots & \Delta\phi_{l,m,l',m'}^I \end{bmatrix}^T$$

$$A = \begin{bmatrix} \alpha & \beta \end{bmatrix}$$

$$\alpha = \begin{bmatrix} \alpha_{l,m}^1 & \alpha_{l,m}^2 & \cdots & \alpha_{l,m}^I \end{bmatrix}^T \tag{4}$$

$$\beta = \begin{bmatrix} \beta_1 & \beta_2 & \cdots & \beta_I \end{bmatrix}^T$$

$$W = \begin{bmatrix} w_{l,m,l',m'}^1 & w_{l,m,l',m'}^2 & \cdots & w_{l,m,l',m'}^I \end{bmatrix}^T$$

where $\Delta\Phi$ is a vector containing phase differences between two adjacent pixels in a total of I interferograms. A is the design matrix including height-to-phase conversion factors and time combination matrix. W is a stochastic vector.

The least squares solution of the observation equations is

$$\begin{bmatrix} \Delta\hat{h}_{l,m,l',m'} \\ \Delta\hat{V} \end{bmatrix} = \left(A^T P^{dd} A\right)^{-1} A^T P^{dd} \Delta\Phi$$

$$\Delta\hat{\Phi} = A\left(A^T P^{dd} A\right)^{-1} A^T P^{dd} \Delta\Phi \tag{5}$$

$$r = \Delta\Phi - A\left(A^T P^{dd} A\right)^{-1} A^T P^{dd} \Delta\Phi$$

where the circumflex ^ denotes estimated quantities; P^{dd} is the weight matrix which can be obtained by taking the inverse of the variance matrix of the double-difference phases and r is the least squares residuals. The corresponding covariance matrices of the estimated quantities are

$$D\left\{\begin{bmatrix} \Delta\hat{h}_{l,m,l',m'} \\ \Delta\hat{V} \end{bmatrix}\right\} = Q_{\hat{x}\hat{x}} = \left(A^T P^{dd} A\right)^{-1}$$

$$D\{\Delta\hat{\Phi}\} = Q_{\Delta\hat{\Phi}\Delta\hat{\Phi}} = A\left(A^T P^{dd} A\right)^{-1} A^T \tag{6}$$

$$D\{r\} = Q_{rr} = Q_{dd} - A\left(A^T P^{dd} A\right)^{-1} A^T.$$

With the outlier detector proposed in Zhang et al. (2011b), the arcs that have phase ambiguities are removed according to the least squares residuals. In Fig. 5, the residuals from an arc with and without phase ambiguities are presented, indicating that the phase ambiguities result in much larger residuals. These clearly distinguishable residuals can help us isolate the arcs with modulo-2π ambiguities. The line-of-sight (LOS) linear deformation rate at arcs can be calculated by updating the design matrix in Eq. (5). After obtaining the parameters (i.e., DEM errors and deformation rates) at arcs we can get the parameters at TCPs by spatial integration with respect to a given reference point, which can also be performed by least squares (Zhang et al., 2011b).

It should be noted that TCPInSAR does not rely on the assumption that the true (i.e. unwrapped) phase gradient at all arcs are within $(-\pi \quad \pi)$. Therefore, even for areas with rapid subsidence, as long as there are enough coherent points, we can apply TCPInSAR to retrieve deformation signals. After constructing a dense network by the local Delaunay triangulation, we can estimate the parameters from arcs and integrate them to the TCP solutions after removing arcs with phase ambiguities. In addition, considering the fact new sensors (e.g. TerraSAR-X and COSMO-Skymed, and future Sentinel-1) can acquire data in rather short repeat intervals, the estimation of phase ambiguities is becoming less necessary in multi-temporal InSAR techniques.
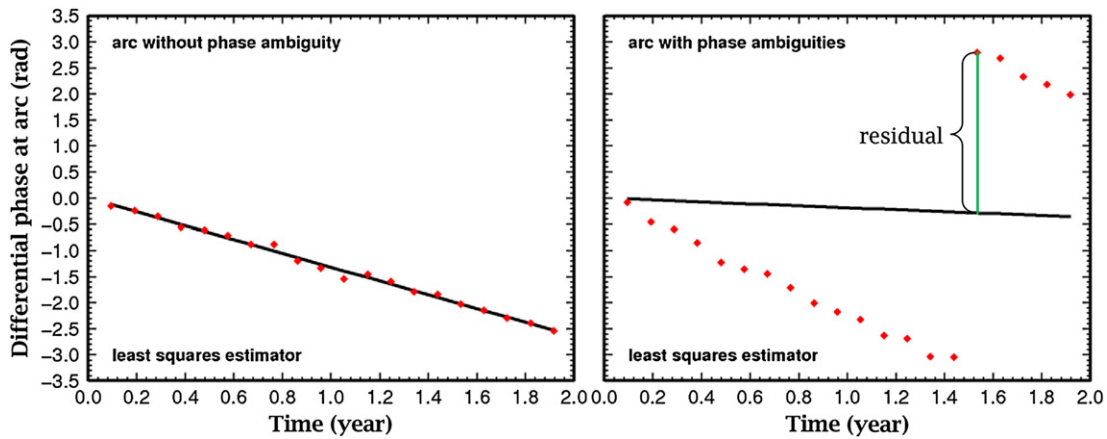
where $\Delta h_{l,\,m,\,l',\,m'}$ is the difference of the topography residuals at two TCPs and $\alpha_{l,m}^i = -\frac{4\pi}{\lambda}\frac{B_{\perp,l,m}^i}{r_{l,m}^i \sin\theta_{l,m}^i}$ is the corresponding coefficient; $\Delta V = \begin{bmatrix} \Delta v_{l,m,l',m'}^1 & \Delta v_{l,m,l',m'}^2 & \cdots & \Delta v_{l,m,l',m'}^J \end{bmatrix}^T$ is the differential deformation rate vector. When linear deformation is assumed, i.e., $\Delta v_{l,\,m,\,l',\,m'}^1 = \Delta v_{l,\,m,\,l',\,m'}^2 = \cdots = \Delta v_{l,\,m,\,l',\,m'}^J = \Delta v_{l,\,m,\,l',\,m'}^{linear}$, the vector ΔV has shrunk to $\Delta v_{l,\,m,\,l',\,m'}^{linear}$ and $\beta_i = -\frac{4\pi}{\lambda}\sum_{k=1}^{C_i-1}(t_k - t_{k-1})$ is the corresponding coefficient; $w_{l,\,m,\,l',\,m'}^i$ includes differential phase related to atmospheric artifact ($\Delta\phi_{atmo,\,l,\,m,\,l',\,m'}^i$), orbital error ($\Delta\phi_{orbit,\,l,\,m,\,l',\,m'}^i$), Doppler centroid difference ($\Delta\phi_{dop,\,l,\,m,\,l',\,m'}^i$), and other noise ($\Delta\phi_{noise,\,l,\,m,\,l'\,m'}^i$). Because the differencing operation can significantly reduce the effects of spatially correlated atmospheric artifacts and baseline errors, $w_{l,\,m,\,l',\,m'}^i$ should be extremely low and can be safely taken as a random variable with an expectation

Fig.5. Residuals arose from least squares at an arc without phase ambiguity (left) and the one with ambiguities (right).

2.4.2. Non-linear deformation rate estimation

After the LOS linear deformation rate has been resolved from a network with dense and short arcs, we only need to focus on retrieving the non-linear components from the least squares residuals in order to determine the full-resolution time series deformation. Since there is no phase ambiguity at the remaining arcs, it is safe to integrate the residuals with respect to a reference point to get the absolute phase residuals. To mitigate the effects of atmospheric errors, it is necessary to apply a spatial and temporal filtering on these phase residuals (Berardino et al., 2002; Blanco et al., 2008; Ferretti, Prati, & Rocca, 2000; Mora, Mallorquí, & Broquetas, 2003). However when designing the filter, the selection of optimized window length (i.e., the triangular window length for the temporal filter and the averaging window length for the spatial filter) is never an easy task, which largely depends on the operator's experience. Once the phase residuals are filtered, the basic observation function for non-linear rate estimation can be written as

$$\varphi_{res} = \beta v_{non} + w_{res} \qquad (7)$$

where φ_{res} is the phase residual vector, β has the same definition as in Eq. (4), v_{non} is the non-linear rate vector containing non-linear rates between time-adjacent acquisitions, and w_{res} is noise vector in the phase residuals. The non-linear rates can still be resolved by least squares. When design matrix β exhibits rank deficiency, its pseudoinverse is employed to get the minimum norm least squares solution (Berardino et al., 2002). For a given TCP, the final full resolution deformation rates (v_{full}) is the sum of linear deformation rate (v_{linear}) and non-linear deformation rates (v_{non}), i.e.,

$$v_{full} = v_{linear} + v_{non} \qquad (8)$$

As a summary the steps involved in our TCPInSAR processing are shown in Fig. 6.

3. Results

3.1. Linear deformation rate

The line-of-sight (LOS) linear deformation rate of TCP (Fig. 7) was first calculated according to Eq. (5). To make a visualized comparison with the result estimated by SBAS method (Casu et al., 2006; Lanari et al., 2004a), we also select the GPS site ELSC from SCIGN as the reference point. The overall pattern of the estimated deformation rate map is consistent with the results presented in (Casu et al., 2006; Lanari et al., 2004a), both of which were resolved from unwrapped phase measurements. The deformation rate map also confirms the conclusion reached by Bawden et al. (2001). In the Los Angeles

Basin long-term deformation rate ranges roughly from 2 mm/year to 16 mm/year. Several factors, such as oil and gas extraction, changes in groundwater storage, unrecoverable inelastic compaction as well as the movement of active faults, are known to contribute to the deformation (Argus et al., 2005; Bawden et al., 2001). The largest linear deformation rate (up to 16 mm/year) occurred in the Wilmington oil field which is the largest oil field in the Los Angeles Basin (Fig. 7). The contrast in displacement rate (Fig. 8) is apparent at two sides of Newport–Inglewood fault (NIF) which forms the western margin of the Los Angeles Basin and has been identified as an active fault zone capable of generating damaging earthquakes. The focal mechanisms and the results of the stress inversion indicate that stress fields along the north and south segments of NIF are different, which may be related to an increase in both north–south and east–west horizontal stresses (Hauksson, 1987; Shaw & Suppe, 1996; Yeats, 1973). The increase in horizontal stress can cause uplift along the fault, which is confirmed by the high-density measurements of LOS uplift rates ranging from 0.4 to 2.4 mm/year along the west side of the NIF (Fig. 8). However it should be noticed that since deformation within the Los Angeles Basin is complicated by anthropogenic contribution to the overall tectonic signal (Bawden et al., 2001). Using GPS and InSAR measurements jointly to determine the tectonic contraction across Los Angeles, Bawden et al. (2001) conclude that much of the deformation near the NIF is associated with groundwater pumping rather than slip.

3.2. Short arc vs. long arc

As mentioned in Section 2.2, shorter arcs have better performance when modeling areas with complex deformation. To understand the effect of arc length on the estimated deformation rate we have conducted here a comparison between the results from longer arcs and short ones. During the network construction, we relax the patch size from 500 m to 1500 m and then perform the local Delaunay triangulation. About 4.9% arcs are longer than 500 m. The difference of deformation rates estimated from these two networks is shown in Fig. 9. We can find that generally the results from network with longer arcs underestimate the subsidence. Especially in the Wilmington oil field that suffers large subsidence, the longer arcs can result in an underestimate of subsidence by ~6 mm/year. This underestimation is mainly due to the seasonal deformation of the Los Angeles Basin, which results from periodic groundwater extraction and replenishment (Bawden et al., 2001). The seasonal oscillation can be seen at longer arcs (Fig. 3), which can bias the least squares estimation. Therefore, in areas with complex spatial–temporal deformation patterns, it is recommended to use relatively short arcs for linear deformation rate estimation.
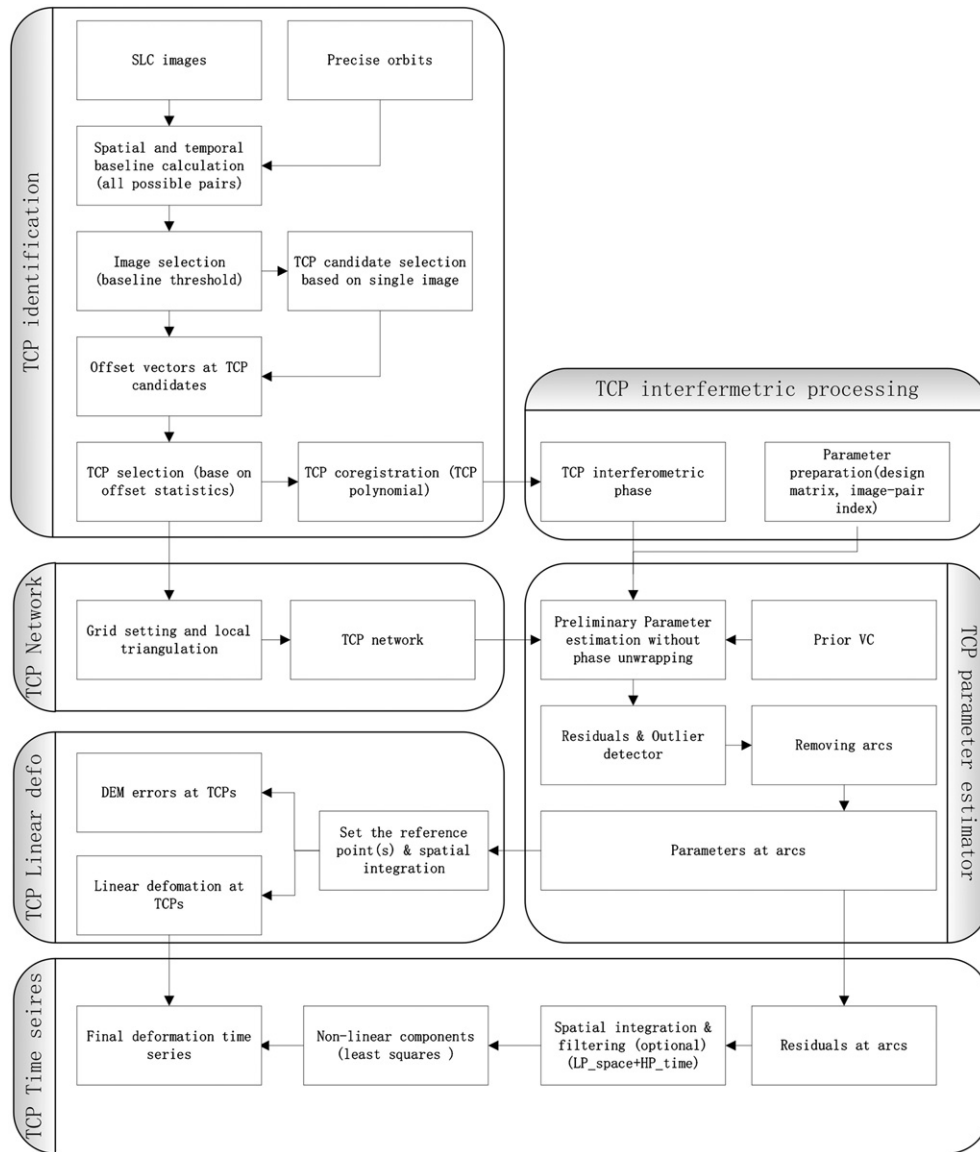
Fig. 6. Flow diagram of the TCPInSAR processing chain.

### 3.3. Solution with smaller datasets

Since the TCPs can be identified interferogram by interferogram, it provides us an opportunity to estimate the deformation parameters with a smaller set of images. This is important for estimating ground surface deformation in areas lacking abundant SAR data. Considering the seasonal oscillation within the Los Angeles Basin, we subsample the interferometric observations by a factor of two, resulting in 27 interferograms. The linear deformation rate map estimated from these evenly subsampled interferograms (Fig. 10) is in good agreement with the one from all of the selected interferograms. The discrepancy, with a mean of 0.14 mm/year and a standard deviation of 0.31 mm/year, suggests that the TCPInSAR approach is also adequate for retrieving deformation signal from a small set of SAR images.

3.4. Deformation time series

As mentioned in Section 2.4.2, before the estimation of deformation time series, space–time filtering is usually performed to suppress the possible effect of atmospheric delays. However, considering the fact that rather short arcs are constructed and the periodic deformation pattern in the Los Angeles Basin is relatively complex, we have

not performed the filtering operation here. The non-linear deformation rates can be resolved from Eq. (6). It should be noted that since the observation at GPS site ELSC started from 1999, the time overlap with the selected SAR data is rather limited, raising difficulties in unifying GPS and TCPInSAR measurements to this reference site. Therefore we have selected another GPS site USC1 with observation starting from 1994 as the reference point to determine the deformation time series. According to Argus et al.(2005), the velocity at site USC1 might have anthropogenic contribution with a magnitude of 0.5 mm/year. This, however, should not affect the comparison between TCPInSAR and GPS measurements since both are tied to the same reference site.

To validate the estimated TCPInSAR results, we select 8 GPS sites from the SCIGN network, most of which were also used in Casu et al.(2006) and Lanari et al.(2004a). We have calculated the standard deviation of the differences between the TCPInSAR measurement and the corresponding LOS-projected GPS time series (Fig. 11). We have selected 32 GPS sites over the study site, all of which have more than 1 year overlapping time with the SAR data (Fig. 1). The average standard deviation of the differences is 4.6 mm, indicating a good agreement between TCPInSAR-derived time series deformation measurements and daily GPS solutions. Moreover, the deformation
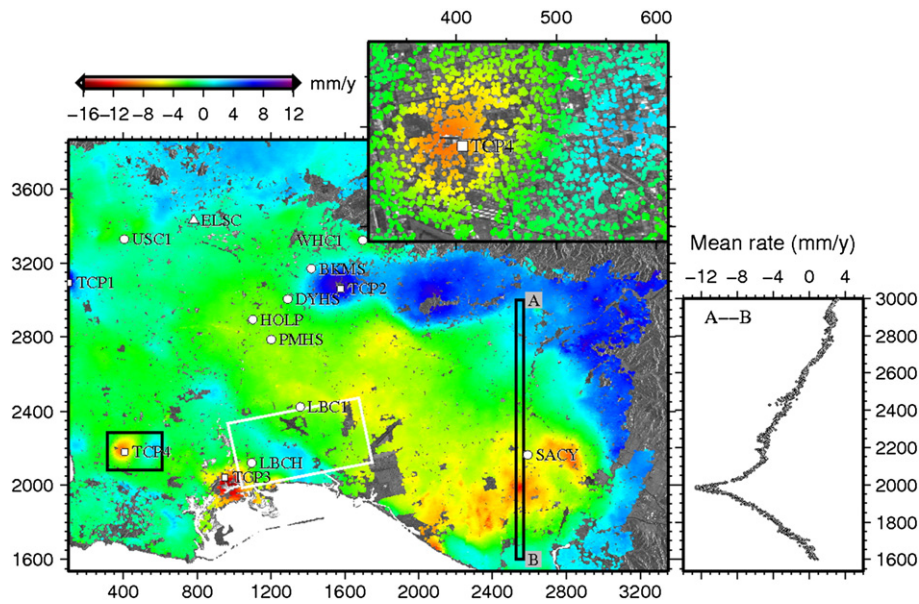
Fig. 7. The long-term deformation rate under the SAR coordinate (unit: pixel of 20 m) estimated by TCPInSAR technique. The red triangle stands for the reference point and the red dots are the GPS sites used for validation. The red squares are TCPs located in oilfields. The inset shows the deformation rate in the gray rectangular area. Deformation rate across profile A–B is also shown. The green box outlines an area near NIF.

at each SAR acquisition time is also compatible with the results presented in Casu et al.(2006) and Lanari et al.(2004a). It should be noted that although the InSAR result we estimated is more consistent with GPS observations than that from SBAS method, the improvement has nothing to do with phase unwrapping errors and we believe it mainly comes from the fact that TCPInSAR uses point pairs (arcs) as observations while SBAS uses points. It is clear that point pairs constructed by neighboring TCPs can better suppress the effect of spatially correlated components of atmospheric errors. Besides the GPS sites, we also select 4 TCPs (Fig. 7) with large linear deformation rates to investigate their time varying deformation patterns. TCP1 locates near the Inglewood oilfield in Baldwin Hills and shows an upward ground motion due to hydrocarbon recovery effort (Bawden et al., 2001). Uplift trend can also be observed on TCP2 in the Santa Fe Springs oilfield, where fluctuations in surface elevation result from changes in injection rates and declining oilfield operations (California Department of Conservation, Oil and Gas Statistics, Annual Report, http://www.conservation.ca.gov). TCP3 and TCP4 are in the Wilmington oilfield

and experienced an elevation loss of about 60 mm from Oct.1995 to Dec. 2000. The deformation time series at TCP3 and TCP4 also indicate that their LOS subsidence rates were occasionally mitigated during the observation time span which might be caused by increasing and realigning water injection (California Department of Conservation, Oil and Gas Statistics, Annual Report, http://www.conservation.ca. gov).

4. Discussions and conclusions

A multi-temporal TCPInSAR technique, including TCP identification, TCP network and TCP least squares estimator, has been presented in this paper. The technique provides a more reliable way to retrieve ground deformation signals with no need of phase unwrapping. Based on the offset deviation and sub-band SAR image processing, our approach can identify dense coherent points from one image pair only, reducing significantly the requirement on a minimum number (about 20 to 30) of SAR images in most PSInSAR
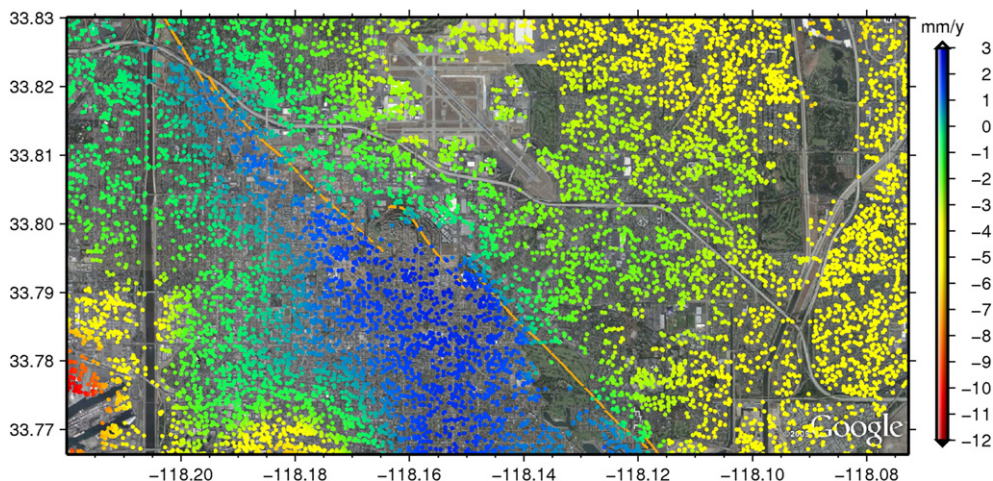
Fig. 8. Deformation rates at two sides of Newport–Inglewood fault (the orange line). The extent of the area is shown in Fig. 7.
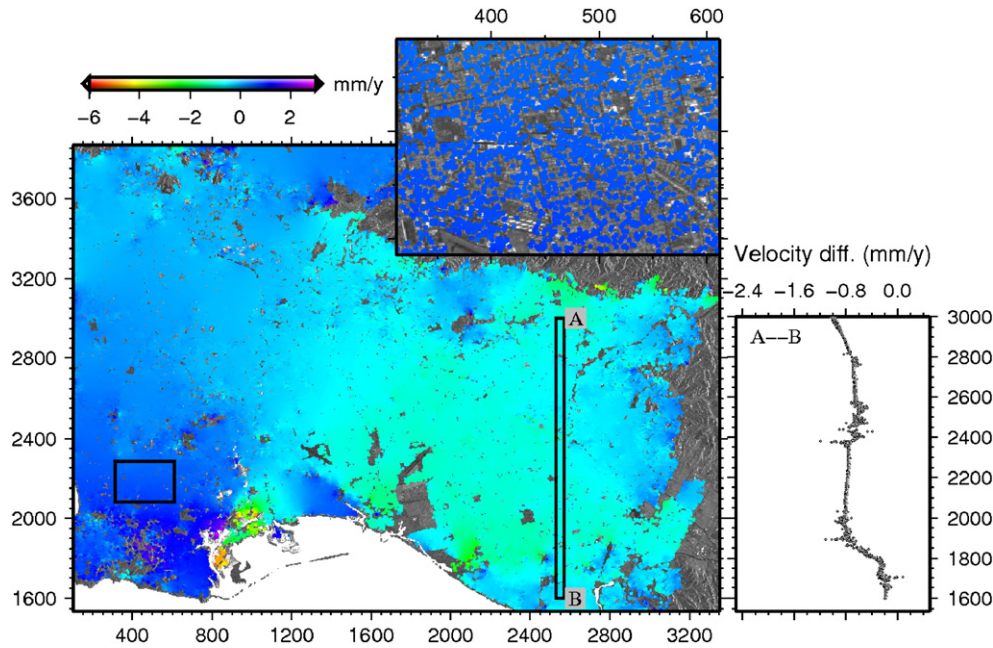
Fig. 9. The difference between deformation rates estimated with short-arc network and long-arc network approaches.

processing methods. With local triangulation network, the selected TCPs can be connected extensively with short arcs. Under the framework of least squares the deformation rate can be estimated from a set of wrapped interferograms. A special attention in TCPInSAR processing is to select proper threshold for the arc length. In areas undergoing complex deformation, if coherent points are densely selected, shorter arcs will render more reliable solutions. However using too short arcs has a risk of separating the network into several blocks, preventing the solution with one reference point. According to the density of TCP and the phase gradient in the interferograms an adaptive arc connection strategy might be a better choice. Finally, we have

applied the TCPInSAR technique to retrieve the long-term ground motion in the Los Angeles Basin. The performance of our method has been examined by the comparison with GPS observations and the previous InSAR results that utilized unwrapped interferograms.

The TCPInSAR measurements, including the linear deformation rate as well as deformation time series, indicate that the deformation pattern in the Los Angeles Basin is dominated by the motion associated with seasonal oscillation of ground water table, and the long term anthropogenic deformation related to activities such as oil pumping, water withdrawal and re-injection as well as tectonic motion of both surface and blind thrust faults. The estimated deformation
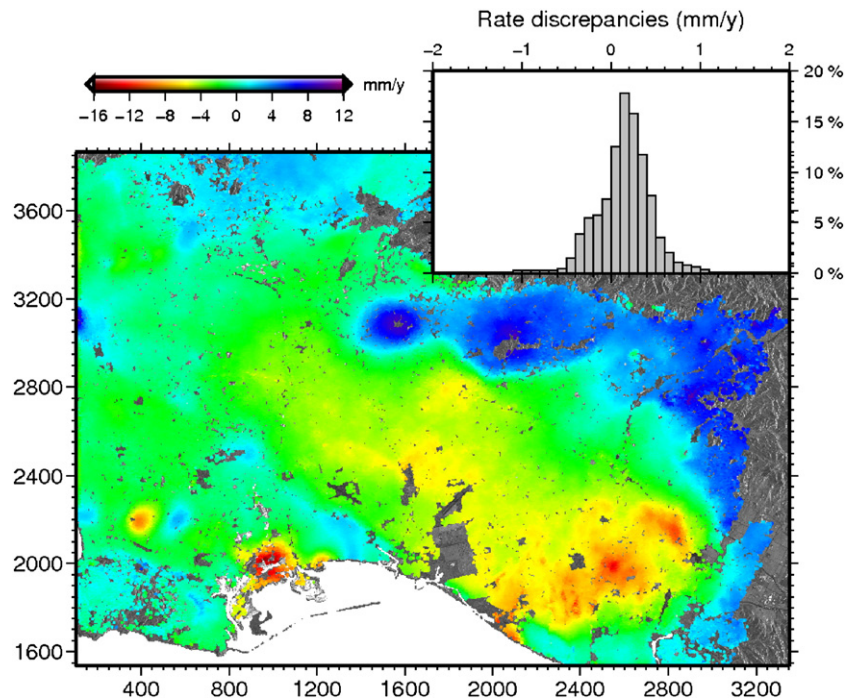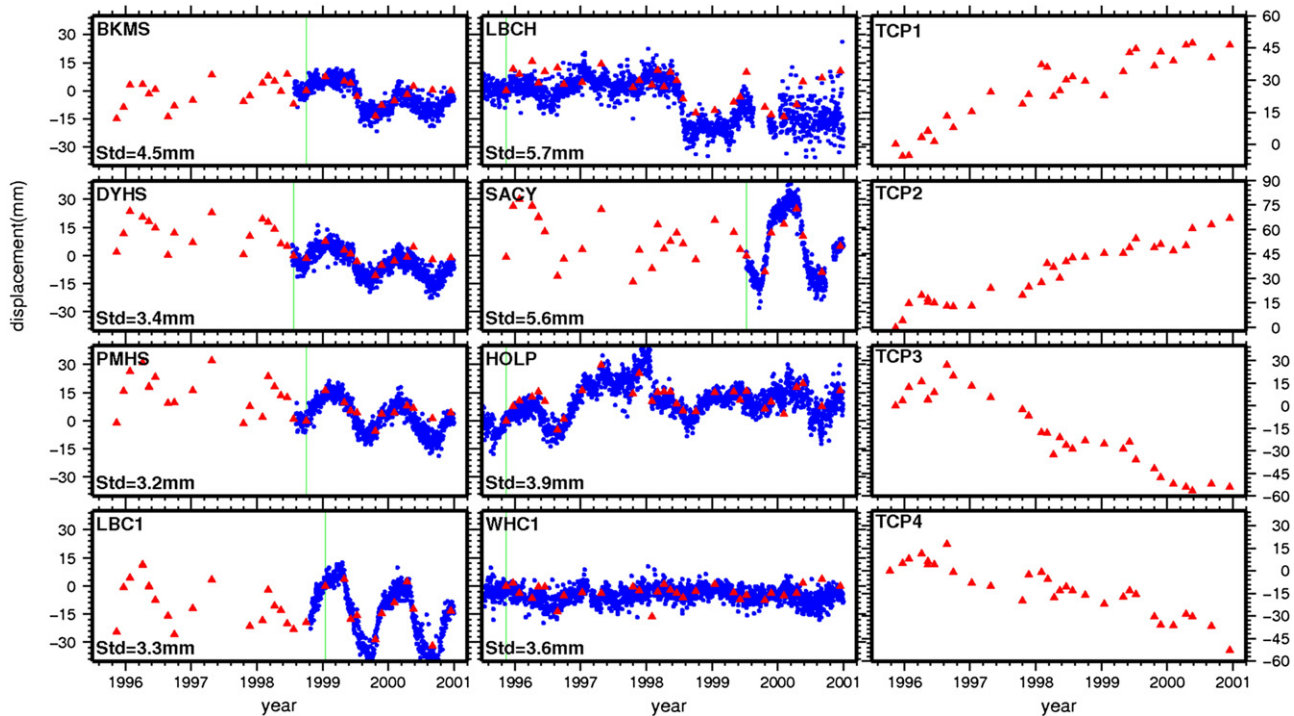

Fig. 10. The LOS linear rate map estimated from half sampled interferograms. The inset shows the histogram of deformation rate discrepancies compared with those from all the interferograms.

Fig. 11. Comparison between TCPInSAR-derived time series deformation (red triangles) and GPS daily observations (blue dots) as well as time varying deformation patterns at 4 TCPs shown in Fig. 7. The GPS measurements are first projected onto the LOS direction according to the unit look vector [0.41, −0.09, 0.91] (east, north, up); and then two sets of measurements (InSAR and GPS) are shifted with respect to the same spatial reference point (USC1) and the reference time (i.e., the green lines). The standard deviation of the discrepancies between InSAR and GPS measurements is also reported.

maps with high spatial resolution are expected to be helpful to assess the earthquake hazards for metropolitan Los Angeles.

References

Argus, D. F., Heflin, M. B., Peltzer, G., Crampe, F., & Webb, F. H. (2005). Interseismic strain accumulation and anthropogenic motion in metropolitan Los Angeles. *Journal of Geophysical Research-Solid Earth, 110*, B04401, doi:10.1029/2003JB002934.

Bamler, R., & Eineder, M. (2005). Accuracy of differential shift estimation by correlation and split-bandwidth interferometry for wideband and Delta-k SAR systems. *IEEE Geoscience and Remote Sensing Letters, 2*, 151–155.

Bawden, G. W., Thatcher, W., Stein, R. S., Hudnut, K. W., & Peltzer, G. (2001). Tectonic contraction across Los Angeles after removal of groundwater pumping effects. *Nature, 412*, 812–815.

Berardino, P., Fornaro, G., Lanari, R., & Sansosti, E. (2002). A new algorithm for surface deformation monitoring based on small baseline differential SAR interferograms. *IEEE Transactions on Geoscience and Remote Sensing, 40*, 2375–2383.

Biggs, J., Burgmann, R., Freymueller, J. T., Lu, Z., Parsons, B., Ryder, I., et al. (2009). The postseismic response to the 2002 M 7.9 Denali Fault earthquake: Constraints from InSAR 2003–2005. *Geophysical Journal International, 176*, 353–367.

Biggs, J., Wright, T., Lu, Z., & Parsons, B. (2007). Multi-interferogram method for measuring interseismic deformation: Denali fault, Alaska. *Geophysical Journal International, 170*, 1165–1179.

Blanco, P., Mallorquí, J. J., Duque, S., & Monells, D. (2008). The Coherent Pixels Technique (CPT): An advanced DInSAR technique for non-linear deformation monitoring. *Pure and Applied Geophysics, 165*, 1167–1193.

Brooks, B. A., Merrifield, M. A., Foster, J., Werner, C. L., Gomez, F., Bevis, M., et al. (2007). Space geodetic determination of spatial variability in relative sea level change, Los Angeles Basin. *Geophysical Research Letters, 34*, L01611, doi:10.1029/2006GL028171.

Casu, F., Manzo, M., & Lanari, R. (2006). A quantitative assessment of the SBAS algorithm performance for surface deformation retrieval from DInSAR data. *Remote Sensing of Environment, 102*, 195–210.

Colesanti, C., Ferretti, A., Prati, C., & Rocca, F. (2003). Monitoring landslides and tectonic motions with the Permanent Scatterers Technique. *Engineering Geology, 68*, 3–14.

Davis, T. L., Namson, J., & Yerkes, R. F. (1989). A cross section of the Los Angeles area: Seismically active fold and thrust belt, the 1987 Whittier Narrows Earthquake and earthquake hazard. *Journal of Geophysical Research, 94*(B7), 9644–9664.

Ferretti, A., Prati, C., & Rocca, F. (2000). Nonlinear subsidence rate estimation using permanent scatterers in differential SAR interferometry. *IEEE Transactions on Geoscience and Remote Sensing, 38*, 2202–2212.

Ferretti, A., Prati, C., & Rocca, F. (2001). Permanent scatterers in SAR interferometry. *IEEE Transactions on Geoscience and Remote Sensing, 39*, 8–20.

Fialko, Y. (2004). Evidence of fluid-filled upper crust from observations of postseismic deformation due to the 1992 M(w)7.3 Landers earthquake. *Journal of Geophysical Research-Solid Earth, 109*, B08401, doi:10.1029/2004JB002985.

Hanssen, R. F. (2001). *Radar interferometry: Data interpretation and error analysis.* : Kluwer Academic Publishers.

Hauksson, E. (1987). Seismotectonics of the Newport–Inglewood fault zone in the Los Angeles Basin, southern California. *Bulletin of the Seismological Society of America, 77*, 539–561.

Hauksson, E. (1990). Earthquakes, faulting, and stress in the Los Angeles Basin. *Journal of Geophysical Research-Solid Earth, 95*(B10), 15,365–15,394, doi:10.1029/JB095iB10p15365.

Hauksson, E., & Jones, L. M. (1989). The 1987 Whittier Narrows earthquake sequence in Los Angeles, southern California: Seismological and tectonic analysis. *Journal of Geophysical Research, 94*(B7), 9569–9589, doi:10.1029/JB094iB07p09569.

Hauksson, E., Jones, L. M., & Hutton, K. (1995). The 1994 Northridge earthquake sequence in California — Seismological and tectonic aspects. *Journal of Geophysical Research-Solid Earth, 100*, 12335–12355.

Hooper, A. (2008). A multi-temporal InSAR method incorporating both persistent scatterer and small baseline approaches. *Geophysical Research Letters, 35*, L16302, doi:10.1029/2008GL034654.

Kampes, B. M. (2006). *Radar interferometry: Persistent scatterer technique.* : Springer.

Lanari, R., Lundgren, P., Manzo, M., & Casu, F. (2004). Satellite radar interferometry time series analysis of surface deformation for Los Angeles, California. *Geophysical Research Letters, 31*, L23613, doi:10.1029/2004GL021294.

Lanari, R., Mora, O., Manunta, M., Mallorqui, J. J., Berardino, P., & Sansosti, E. (2004). A small-baseline approach for investigating deformations on full-resolution

differential SAR interferograms. *IEEE Transactions on Geoscience and Remote Sensing, 42*, 1377–1386.

Lauknes, T. R., Zebker, H. A., & Larsen, Y. (2011). InSAR Deformation Time Series Using an L1-Norm Small-Baseline Approach. *IEEE Transactions on Geoscience and Remote Sensing, 49*(1), 536–546.

Li, Z. H., Fielding, E. J., & Cross, P. (2009). Integration of InSAR time-series analysis and water-vapor correction for mapping postseismic motion after the 2003 Bam (Iran) earthquake. *IEEE Transactions on Geoscience and Remote Sensing, 47*, 3220–3230.

Lu, Z., Dzurisin, D., Biggs, J., Wicks, C., & McNutt, S. (2010). Ground surface deformation patterns, magma supply, and magma storage at Okmok volcano, Alaska, from InSAR analysis: 1. Intereruption deformation, 1997–2008. *Journal of Geophysical Research-Solid Earth, 115*, B00B02, doi:10.1029/2009JB006969.

Mellors, R. J., Magistrale, H., Earle, P., & Cogbill, A. (2004). Comparison of four moderate-size earthquakes in southern California using seismology and InSAR. *Bulletin of the Seismological Society of America, 94*, 2004–2014.

Mora, O., Mallorquí, J. J., & Broquetas, A. (2003). Linear and nonlinear terrain deformation maps from a reduced set of interferometric SAR images. *IEEE Transactions on Geoscience and Remote Sensing, 41*, 2243–2253.

Shaw, J. H., & Shearer, P. M. (1999). An elusive blind thrust fault beneath metropolitan Los Angeles. *Science, 283*, 1516–1518.

Shaw, J. H., & Suppe, J. (1996). Earthquake hazards of active blind-thrust faults under the central Los Angeles Basin, California. *Journal of Geophysical Research-Solid Earth, 101*, 8623–8642.

U.S. Geological Survey (2010). Quaternary fault and fold database for the United States. accessed Mar 1, 2011, from USGS web site: http://earthquake.usgs.gov/hazards/qfaults/

Wald, D. J., & Graves, R. W. (1998). The seismic response of the Los Angeles Basin, California. *Bulletin of the Seismological Society of America, 88*, 337–356.

Watson, K. M., Bock, Y., & Sandwell, D. T. (2002). Satellite interferometric observations of displacements associated with seasonal groundwater in the Los Angeles Basin. *Journal of Geophysical Research-Solid Earth, 107*, 2074, doi:10.1029/2001JB000470.

Wright, T. L. (1991). Structural geology and tectonic evolution of the Los Angeles Basin. In K. T. Biddle (Ed.), *Active margin basins. American Association of Petroleum Geologists Memoir, 52*. (pp. 35–134).

Wright, T., Parsons, B., & Fielding, E. (2001). Measurement of interseismic strain accumulation across the North Anatolian Fault by satellite radar interferometry. *Geophysical Research Letters, 28*, 2117–2120.

Yeats, R. S. (1973). Newport–Inglewood fault zone, Los Angeles, California. *American Association of Petroleum Geologists Bulletin, 57*, 117–135.

Yerkes, R. F., McCulloh, T. H., Schoellhamer, J. E., & Vedder, J. G. (1965). Geology of the Los Angeles Basin, California: An introduction. *U.S. Geology Survey Professional Paper, 0420-A*. (pp. A1–A57).

Zhang, L., Ding, X. L., & Lu, Z. (2011). Ground settlement monitoring based on temporarily coherent points between two SAR acquisitions. *ISPRS Journal of Photogrammetry and Remote Sensing, 66*, 146–152.

Zhang, L., Ding, X. L., & Lu, Z. (2011). Modeling PSInSAR time series without phase unwrapping. *IEEE Transactions on Geoscience and Remote Sensing, 49*, 547–556.

Zhang, L., Ding, X. L., & Lu, Z. (2011). Deformation rate estimation on changing landscapes using Temporarily Coherent Point InSAR. *Proceedings of Fringe 2011* 9 pp., Frascati, Italy.